IOP PUBLISHING CLASSICAL AND QUANTUM GRAVITY

Class. Quantum Grav. **24** (2007) S43–S58 doi:10.1088/0264-9381/24/12/S05

Binary black holes on a budget: simulations using workstations

Pedro Marronetti[1], Wolfgang Tichy[1], Bernd Brügmann[2], Jose González[2], Mark Hannam[2], Sascha Husa[2] and Ulrich Sperhake[2]

[1] Department of Physics, Florida Atlantic University, Boca Raton, FL 33431, USA
[2] Theoretical Physics Institute, University of Jena, 07743 Jena, Germany

E-mail: pmarrone@fau.edu

Received 22 January 2007, in final form 8 May 2007
Published 30 May 2007
Online at stacks.iop.org/CQG/24/S43

Abstract

Binary black hole simulations have traditionally been computationally very expensive: current simulations are performed in supercomputers involving dozens if not hundreds of processors, thus systematic studies of the parameter space of binary black hole encounters still seem prohibitive with current technology. Here we show how the multi-layered refinement level code BAM can be used on dual processor workstations to simulate certain binary black hole systems. BAM, based on the moving punctures method, provides grid structures composed of boxes of increasing resolution near the centre of the grid. In the case of binaries, the highest resolution boxes are placed around each black hole and they track them in their orbits until the final merger when a single set of levels surrounds the black hole remnant. This is particularly useful when simulating spinning black holes since the gravitational fields gradients are larger. We present simulations of binaries with equal mass black holes with spins parallel to the binary axis and intrinsic magnitude of $S/m^2 = 0.75$. Our results compare favourably to those of previous simulations of this particular system. We show that the moving punctures method produces stable simulations at maximum spatial resolutions up to $M/160$ and for durations of up to the equivalent of 20 orbital periods.

PACS numbers: 04.30.Db, 04.25.Dm, 97.80.Fk

(Some figures in this article are in colour only in the electronic version)

1. Introduction

As the latest generation of gravitational wave detectors becomes operational, the problem of faithfully simulating the evolution of binary systems of compact objects, black holes in

particular, has become increasingly important. While post-Newtonian (PN) approximations can be used in the first stages of the life of a binary black hole (BBH), when the two objects get close and are rapidly orbiting around each other, only solutions to the full nonlinear Einstein equations can provide the desired level of precision. Due to the complexity of such equations, these solutions can only be achieved by means of numerical algorithms. These results are of particular interest for laser-interferometric observatories since BBH will be highly relativistic when entering the sensitivity range of the detectors.

Such simulations pose a hard and challenging problem. Until recently they tended to fail after a very short time due to instabilities [25] which resulted in exponentially growing run-away solutions. Fortunately, tremendous progress has been achieved over the last two years [3–5, 11–16, 22, 24, 32, 33, 42]. Within the moving puncture approach and also with the generalized harmonic system, it is now possible to evolve BBH systems through several orbits and the subsequent merger and ringdown phases.

Stable and accurate, modern BBH simulations require large computer resources and even modest size runs are performed on supercomputers involving dozens or even hundreds of processors. The goal of this paper is to showcase the ability of the code BAM [12] to evolve certain BBH systems on workstations, providing results of comparable quality to those obtained in simulations using much larger computer systems. Workstations with similar characteristics to the ones used here are reasonably affordable (less than $3000 USD at the time of publication). BAM provides grid structures composed of boxes of increasing resolution near the centre of the grid. In the case of binaries, the highest resolution boxes are placed around each black hole. The boxes track the holes in their orbits until the final merger, when a single set of levels surround the black hole remnant. A direct consequence of this grid structure is the efficient use of computational resources, as will be detailed in section 3. BAM currently handles fourth-order accurate evolutions.

The end result of a BBH merger is a larger black hole. This final black hole could in principle be non-spinning, however the conditions for this to occur are very unlikely: any astrophysically realistic scenario would lead to a spinning object. We test BAM by simulating a BBH with identical black holes with intrinsic spins $S/m = 0.75$ parallel to the orbital angular momentum. We choose high-spin binaries since they require very high resolution near the black holes which is currently difficult to achieve for most numerical codes of this type. The time evolution of the BBH system is achieved through the moving punctures method [3, 13].

In order to test the quality and accuracy of the simulations, we concentrate on the measurement of the final black hole mass and angular momentum. To do that, we implemented algorithms based on the conversion of surface integrals (at the core of the definition of the ADM mass and angular momentum) to volume integrals using Gauss's theorem. These calculations are studied and compared with alternative ways of measuring these global quantities.

Section 2 presents a brief description of the equations and the initial data sets and describes the details of a BAM's numerical grid structure [12] and the algorithms used to calculate the mass and angular momentum. Sections 3 and 4 present performance and convergence tests, respectively. Section 4.2 compares alternative calculations of the mass and angular momentum, and our results are discussed in section 5.

2. Evolution using the moving punctures method

2.1. Initial data

In order to start our simulations we need initial data for spinning BBH with equal masses and spins. Since we will employ the moving punctures approach in our evolutions we will use

Table 1. Initial data parameters. Here m_b is the bare mass parameter of each puncture and $M = 2m$ is the sum of the ADM masses m measured at each puncture. The holes have coordinate separation D, with puncture locations $(0, \pm D/2, 0)$, linear momenta $(\mp P, 0, 0)$, and spins $(0, 0, S)$ with $S/m^2 = 0.75$. We also list the 2PN estimates for the ADM mass $M_\infty^{\rm ADM}$, the ADM angular momentum $J_\infty^{\rm ADM}$ and the angular velocity Ω. These quantities are shown using two different scaling factors (M and $M_\infty^{\rm ADM}$) for easier comparison with work done by other groups.

m_b/M	$D/2M$	P/M	S/M^2	$M_\infty^{\rm ADM}/M$	$J_\infty^{\rm ADM}/M^2$	$M\Omega$
0.325 55	3.0000	0.127 56	0.187 50	0.983 13	1.140 34	0.055 502
$m_b/M_\infty^{\rm ADM}$	$D/2M_\infty^{\rm ADM}$	$P/M_\infty^{\rm ADM}$	$S/M_\infty^{\rm ADM2}$	$M/M_\infty^{\rm ADM}$	$J_\infty^{\rm ADM}/M_\infty^{\rm ADM2}$	$M^{\rm ADM}\Omega$
0.331 14	3.0515	0.129 75	0.193 99	1.017 16	1.179 81	0.054 566

standard puncture initial data [10] with the momentum and spin parameters in the extrinsic curvature given by 2PN estimates [26]. It is sufficient to use 2PN estimates because standard puncture data are inconsistent with PN theory beyond $(v/c)^3$ [38, 44, 45]. These parameters along with 2PN estimates for ADM mass $M_\infty^{\rm ADM}$, ADM angular momentum $J_\infty^{\rm ADM}$ and angular velocity Ω are shown in table 1.

The coordinate distance D and the momentum and spin parameters P and S directly enter the Bowen–York extrinsic curvature, while the bare mass parameter is obtained from the condition that the ADM masses measured at each puncture should be $m = M/2$. This implies that each black hole has an individual spin of $\frac{S}{m^2} = \frac{S}{(M/2)^2} = 0.75$, where as in [2, 39, 40] we assume that m is a good approximation for the initial individual black hole masses. Note that these data are very close to the values used by Campanelli *et al* [15]. If we express everything in terms of the PN ADM mass, the largest difference is that our bare mass parameter is about 1% lower.

To complete the definition of the initial data, we also need to specify initial values for the lapse α and shift vector β^i. At time $t = 0$, we use

$$\alpha = \left(1 + \frac{m_b}{r_1} + \frac{m_b}{r_2}\right)^{-2}, \qquad \beta^i = 0,$$

where r_A is the coordinate distance from puncture A. Both lapse and shift are updated by evolution equations depending on the physical variables, as described below.

2.2. *Evolution of gravitational fields*

We evolve the initial data with the BSSN system [6, 35]. In the case of BSSN, the 3-metric g_{ij} is written as

$$g_{ij} = \mathrm{e}^{4\phi}\tilde{g}_{ij},$$

where the conformal metric $\tilde{g}_{ij}$ has unit determinant. In addition, the extra variable

$$\tilde{\Gamma}^i = -\partial_j \tilde{g}^{ij}$$

is introduced where $\tilde{g}^{ij}$ is the inverse of the conformal metric. Furthermore, the extrinsic curvature is split into its trace free part $\tilde{A}_{ij}$ and its trace K, and given by

$$K_{ij} = \mathrm{e}^{4\phi}\left(\tilde{A}_{ij} + \frac{K}{3}\tilde{g}_{ij}\right).$$

These variables are evolved using

$$\partial_0\phi = -\tfrac{1}{6}\alpha K, \qquad \partial_0\tilde{g}_{ij} = -2\alpha\tilde{A}_{ij},$$
$$\partial_0\tilde{A}_{ij} = \mathrm{e}^{-4\phi}[-D_iD_j\alpha + \alpha R_{ij}]^{\mathrm{TF}} + \alpha\big(K\tilde{A}_{ij} - 2\tilde{A}_{ik}\tilde{A}^k{}_j\big),$$
$$\partial_0 K = -D^iD_i\alpha + \alpha\big(\tilde{A}_{ij}\tilde{A}^{ij} + \tfrac{1}{3}K^2\big),$$
$$\partial_t\tilde{\Gamma}^i = \tilde{g}^{ij}\partial_j\partial_k\beta^i + \tfrac{1}{3}\tilde{g}^{ij}\partial_j\partial_k\beta^k + \beta^j\partial_j\tilde{\Gamma}^i - \tilde{\Gamma}^j\partial_j\beta^i + \tfrac{2}{3}\tilde{\Gamma}^i\partial_j\beta^j - 2\tilde{A}^{ij}\partial_j\alpha$$
$$+2\alpha\left(\tilde{\Gamma}^i_{jk}\tilde{A}^{jk} + 6\tilde{A}^{ij}\partial_j\phi - \tfrac{2}{3}\tilde{g}^{ij}\partial_j K\right),$$

where $\partial_0 = \partial_t - \mathcal{L}_\beta$, D_i is the covariant derivative with respect to the conformal metric $\tilde{g}_{ij}$, and 'TF' denotes the trace-free part of the expression with respect to the *physical* metric, $X^{\mathrm{TF}}_{ij} = X_{ij} - \frac{1}{3}g_{ij}X^k_k$. The Ricci tensor R_{ij} is given by

$$R_{ij} = \tilde{R}_{ij} + R^\phi_{ij}$$
$$\tilde{R}_{ij} = -\tfrac{1}{2}\tilde{g}^{lm}\partial_l\partial_m\tilde{g}_{ij} + \tilde{g}_{k(i}\partial_{j)}\tilde{\Gamma}^k + \tilde{\Gamma}^k\tilde{\Gamma}_{(ij)k} + \tilde{g}^{lm}\left(2\tilde{\Gamma}^k_{l(i}\tilde{\Gamma}_{j)jm} + \tilde{\Gamma}^k_{im}\tilde{\Gamma}_{klj}\right),$$
$$R^\phi_{ij} = -2D_iD_j\phi - 2\tilde{g}_{ij}D^kD_k\phi + 4D_i\phi D_j\phi - 4\tilde{g}_{ij}D^k\phi D_k\phi.$$

The Lie derivatives of the tensor densities ϕ, $\tilde{g}_{ij}$ and $\tilde{A}_{ij}$ (with weights $1/6$, $-2/3$ and $-2/3$) are

$$\mathcal{L}_\beta\phi = \beta^k\partial_k\phi + \tfrac{1}{6}\partial_k\beta^k,$$
$$\mathcal{L}_\beta\tilde{g}_{ij} = \tilde{g}_{ij}\partial_k\tilde{g}_{ij} + \tilde{g}_{ik}\partial_j\beta^k + \tilde{g}_{jk}\partial_i\beta^k - \tfrac{2}{3}\tilde{g}_{ij}\partial_k\beta^k,$$
$$\mathcal{L}_\beta\tilde{A}_{ij} = \tilde{A}_{ij}\partial_k\tilde{A}_{ij} + \tilde{A}_{ik}\partial_j\beta^k + \tilde{A}_{jk}\partial_i\beta^k - \tfrac{2}{3}\tilde{A}_{ij}\partial_k\beta^k.$$

As in [12, 41] we evolve the BSSN system as a partially constrained scheme, where both the algebraic constraints $\det(g) = 1$ and $\mathrm{Tr}(A_{ij}) = 0$ are enforced at every intermediate time step of the evolution scheme. In addition, we also impose the first-order differential constraint $\tilde{\Gamma}^i = -\partial_j\tilde{g}^{ij}$ by replacing all undifferentiated occurrences of $\tilde{\Gamma}^i$ by $-\partial_j\tilde{g}^{ij}$ instead of using the evolved variable $\tilde{\Gamma}^i$.

Note that for puncture initial data the BSSN variable ϕ has a divergence of the form $\log r_A$ at each puncture. Since a logarithmic divergence is relatively weak, the moving-puncture approach consists of simply ignoring this divergence by putting it between grid points at the initial time. One option is to simply evolve the resulting initial data using a finite differencing scheme, which effectively smooths out any divergences, obviating the need for any special treatment of the punctures. This is the approach we have followed in our so-called *P*-runs. Another option is to replace the BSSN variable ϕ by a new variable [13]

$$\chi = \mathrm{e}^{-4\phi},$$

which initially goes like r_A^4 at puncture A. We use this second option in our *C*-runs.

The second ingredient in the moving-puncture method is a modification to the gauge choice. We use a '1 + log' lapse of the form [13]

$$(\partial_t - \beta^i\partial_i)\alpha = -2\alpha K.$$

For the shift, we use the gamma-freezing condition [1, 13]

$$\partial_t\beta^i = \tfrac{3}{4}B^i, \qquad \partial_t B^i = \partial_t\tilde{\Gamma}^i - \eta B^i, \tag{1}$$

with $\eta = 1.0/M$ for the *P*-runs. For the *C*-runs we used the modified gamma-freezing condition

$$(\partial_t - \beta^k\partial_k)\beta^i = \tfrac{3}{4}B^i, \qquad (\partial_t - \beta^k\partial_k)B^i = (\partial_t - \beta^k\partial_k)\tilde{\Gamma}^i - \eta B^i, \tag{2}$$

where advection terms have been added to all time derivatives, and where we choose $\eta = 2.0/M$.

2.3. Measurement of the mass and angular momentum

The black hole resulting from a BBH merger is defined by its mass and angular momentum, thus an accurate measurement of such global gauge-independent quantities becomes critical. One way to estimate these quantities is evaluating the ADM mass and angular momentum after the merger. They are defined as surface integrals on a surface arbitrarily far from the system [9, 30]

$$M^{\mathrm{ADM}} = \frac{1}{16\pi} \oint_{\infty} (\partial_l g_{mr} - \partial_m g_{lr}) g^{nm} g^{lr} \, \mathrm{d}S_n, \tag{3}$$

$$J_i^{\mathrm{ADM}} = \frac{1}{8\pi} \epsilon_{il}^{m} \oint_{\infty} x^l A_m^n \, \mathrm{d}S_n, \tag{4}$$

where ϵ_{ij}^{k} is the Levi-Civita tensor and $\mathrm{d}S_n \equiv \frac{1}{2}\sqrt{g}\epsilon_{nlm}\,\mathrm{d}x^l\,\mathrm{d}x^m$. The estimation of the final black hole parameters in numerical codes is currently done in several different ways: (1) by evaluating equations (3), (4) as far as the grid size permits, (2) by measuring properties of the apparent, event or isolated horizons (see for instance [17, 34]), (3) by estimating the amount of emitted energy and angular momentum in the form of gravitational radiation or (4) by converting the surface integrals (3), (4) to volume integrals using Gauss's theorem. This last method, which has been successfully employed in accretion disks around black holes (see for instance [20, 21]), binary neutron star systems [18, 27–29, 36] and single black hole spacetimes [43], is employed here and compared with results obtained from some of the other techniques. Some of the advantages of this method are (1) the reduction of the influence of noise generated at the outer boundaries, (2) the reduction of gauge drift effects, (3) it provides a real-time quality control factor at all times during the simulation and (4) it complements, and sometimes improves, the accuracy of alternative measurements. These advantages will be clarified in the following section with examples and comparison with some of the alternative methods. All the formulae used here are in Cartesian coordinates. The derivations in this section follow those of Yo *et al* [43] and Duez [19].

Since we are interested in applying these equations in formalisms that perform a conformal decomposition of the physical metric $g_{ij} = \mathrm{e}^{4\phi}\bar{g}_{ij}$, it is useful to transform them accordingly. Following [43], equation (3) can be re-written as

$$\begin{aligned} M^{\mathrm{ADM}} &= \frac{1}{16\pi} \oint_{\infty} [\mathrm{e}^{\phi}(\partial_l \bar{g}_{mr} - \partial_m \bar{g}_{lr}) + 4(\partial_l \mathrm{e}^{\phi} \bar{g}_{mr} - \partial_m \mathrm{e}^{\phi} \bar{g}_{lr})]\, \mathrm{e}^{\phi} \bar{g}^{nm} \bar{g}^{lr} \, \mathrm{d}\bar{S}_n \\ &= \frac{1}{16\pi} \oint_{\infty} [\bar{g}^{lr}(\partial_l \bar{g}_{mr} - \partial_m \bar{g}_{lr}) - 8\partial_m \mathrm{e}^{\phi}] \bar{g}^{nm} \, \mathrm{d}\bar{S}_n \\ &= \frac{1}{16\pi} \oint_{\infty} (\bar{\Gamma}^n - \bar{\Gamma}^{ln}{}_{l} - 8\bar{D}^n \mathrm{e}^{\phi}) \, \mathrm{d}\bar{S}_n, \end{aligned} \tag{5}$$

with $\mathrm{d}\bar{S}_n \equiv \frac{1}{2}\sqrt{\bar{g}}\epsilon_{nlm}\,\mathrm{d}x^l\,\mathrm{d}x^m$, $\bar{\Gamma}^i_{jk}$ the conformal affine connections, $\bar{\Gamma}^i \equiv -\partial_j \bar{g}^{ij}$ and $\bar{D}_n$ the covariant derivative with respect to the conformal spatial metric. Similarly, equation (4) becomes

$$J_i^{\mathrm{ADM}} = \frac{1}{8\pi} \epsilon_{il}^{m} \oint_{\infty} x^l \bar{A}_m^n \, \mathrm{d}\bar{S}_n. \tag{6}$$

Note that we have not assumed that $\sqrt{\bar{g}} = 1$, as is the case in the BSSN formalism.

The method studied in this paper straightforwardly converts these surface integrals using Gauss's law with the only provision of excluding the parts of the grid immediately surrounding the black holes. For an arbitrary vector field f_i, Gauss's law adopts the form

$$\oint_{\infty} f^n \, \mathrm{d}S_n = \int_{V_\infty} \partial_n(\sqrt{g} f^n) \, \mathrm{d}x^3 + \sum_k \oint_{\partial\Omega_k} f^n \, \mathrm{d}S_n, \tag{7}$$

where the first term represents the volume integral over all space except the parts enclosed by the closed surfaces $\partial\Omega_k$ that surround each one of the k black holes. Numerical simulations like ours are performed using grids that cover a finite spatial volume V. Because of that, we can only provide estimates to the quantities defined in equations (5), (6). We will call the calculations of the mass and angular momentum performed in our finite grid volumes M_V and J_V, respectively. After the merger, the gravitational fields settle down in the Kerr geometry corresponding to the final black hole. Once this occurs, the values of M_V and J_V should approximate the corresponding mass and angular momentum of the black hole remnant. The convergence of this approximation is studied in the following section.

In the case of the mass formula (5), the direct application of (7) plus some algebra leads to

$$M_V = \frac{1}{16\pi}\int_V \left(\bar{R} + \bar{\Gamma}^n \bar{\Gamma}^l{}_{nl} - \bar{\Gamma}^{lnm}\bar{\Gamma}_{nlm} - 8\bar{D}^2\,\mathrm{e}^{\phi}\right)\sqrt{\bar{g}}\,\mathrm{d}^3x + \frac{1}{16\pi}\sum_k \oint_{\partial\Omega_k}\left(\bar{\Gamma}^n - \bar{\Gamma}^{nl}{}_l - 8\bar{D}^n\,\mathrm{e}^{\phi}\right)\mathrm{d}\bar{S}_n, \tag{8}$$

where $\bar{R}$ is the spatial Ricci scalar, $\bar{D}^2 \equiv \bar{g}^{mn}\bar{D}_m\bar{D}_n$, and the infinite volume V_∞ has been replaced by the finite volume V. The final step in the derivation of the mass formula is the use of the Hamiltonian constraint

$$\bar{D}^2\,\mathrm{e}^{\phi} = \frac{\mathrm{e}^{\phi}}{8}\bar{R} + \frac{\mathrm{e}^{5\phi}}{12}K^2 - \frac{\mathrm{e}^{5\phi}}{8}\bar{A}^{mn}\bar{A}_{mn},$$

to eliminate in equation (8) the term proportional to $\bar{D}^2\,\mathrm{e}^{\phi}$:

$$M_V = \frac{1}{16\pi}\int_V \left[(1-\mathrm{e}^{\phi})\bar{R} + \bar{\Gamma}^n\bar{\Gamma}^l{}_{nl} - \bar{\Gamma}^{lnm}\bar{\Gamma}_{nlm} + \mathrm{e}^{5\phi}\left(\bar{A}^{mn}\bar{A}_{mn} - \frac{2}{3}K^2\right)\right]\sqrt{\bar{g}}\,\mathrm{d}^3x + \frac{1}{16\pi}\sum_k \oint_{\partial\Omega_k}\left(\bar{\Gamma}^n - \bar{\Gamma}^{nl}{}_l - 8\bar{D}^n\,\mathrm{e}^{\phi}\right)\mathrm{d}\bar{S}_n. \tag{9}$$

In a similar manner, equation (6) is converted to

$$J_{iV} = \frac{1}{8\pi}\epsilon^m_{il}\int_V \left[\mathrm{e}^{6\phi}\bar{A}^l{}_m + x^l\bar{D}_n\left(\mathrm{e}^{6\phi}\bar{A}^n{}_m\right) - \frac{1}{2}\mathrm{e}^{6\phi}x^l\bar{A}_{ns}\partial_m\bar{g}^{ns}\right]\mathrm{d}^3x + \frac{1}{8\pi}\epsilon^m_{il}\sum_k\oint_{\partial\Omega_k} x^l\bar{A}^n_m\,\mathrm{d}\bar{S}_n. \tag{10}$$

The momentum constraint

$$\bar{D}_n\left(\mathrm{e}^{6\phi}\bar{A}^n{}_m\right) = \tfrac{2}{3}\,\mathrm{e}^{6\phi}\bar{D}_m K$$

is now used in equation (10), resulting in

$$J_{iV} = \frac{1}{8\pi}\epsilon^m_{il}\int_V \mathrm{e}^{6\phi}\left[\bar{A}^l{}_m + \frac{2}{3}x^l\bar{D}_m K - \frac{1}{2}x^l\bar{A}_{ns}\partial_m\bar{g}^{ns}\right]\mathrm{d}^3x + \frac{1}{8\pi}\epsilon^m_{il}\sum_k\oint_{\partial\Omega_k} x^l\bar{A}^n_m\,\mathrm{d}\bar{S}_n. \tag{11}$$

Our calculations were based on the BSSN formalism for which the conformal transformation $g_{ij} = \mathrm{e}^{4\phi}\tilde{g}_{ij}$ is such that $\phi \equiv \ln(\tilde{g}^{1/12})$. This condition imposes the algebraic constraints $\tilde{g} = 1$ and $\tilde{\Gamma}^l{}_{nl} = 0$ which can be used to simplify even more equations (9) and (11). These equations are the formulae used in this paper with the 'bar' fields replaced by the corresponding BSSN (tilde) counterparts.

Figure 1 shows the schematics of a typical grid structure. The darker shading indicates higher resolution. In order to avoid the coordinate singularity in the calculation of M_V and

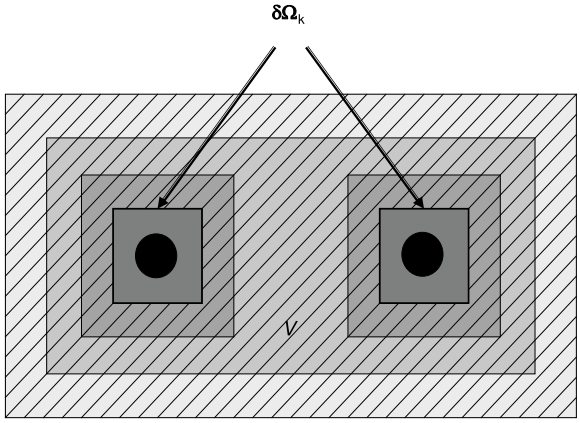

Figure 1. Schematic diagram of BAM's grid structure.

J_V, we exclude the region surrounding the black holes. Given BAM's mesh structure, it is particularly simple to choose the outer edge of one of the moving boxes (the innermost in figure 1) as the boundary $\partial\Omega_k$. In the following section, we provide results for different choices of these boundaries. Both numerical integrations (volume and surface) are performed using an extended version of the trapezoidal rule with fourth-order convergence [31].

3. Code performance

The numerical results discussed in this paper were obtained with the BAM code [11, 12]. This code is based on a method of lines approach using fourth-order finite differencing in space and explicit fourth-order Runge–Kutta (RK) time stepping. For efficiency, Berger–Oliger-type mesh refinement is used [8]. The numerical domain is represented by a hierarchy of nested Cartesian boxes. The hierarchy consists of $L + 1$ levels of refinement, indexed by $l = 0, \ldots, L$. A refinement level consists of one or two Cartesian boxes with a constant grid spacing $h_l = h_0/2^l$ on level l. We have used here $L = 9$ to 11 for the number of refinement levels, with the levels 0 through 5 each consisting of a single fixed box centred on the origin (the centre of mass). On each of the finer levels 6 through L, we initially use two sets of moving boxes centred on each black hole. When the black holes get close enough that the two of these boxes start touching, they are replaced by a single box. The position of each hole is tracked by integrating the shift vector. We have used this same setup with different resolutions to perform convergence tests. The notation used to describe these grid setups is as follows: the $C1$ run is represented by

- $C1$: $\chi_{\eta=2}[5 \times 40 : 6 \times 80][h_{10} = M/56.9 : OB = 729M]$,

where χ represents the use of that dynamical variable, η is the free parameter in the shift vector formula, 5×40 indicates that we have five levels with moving boxes of $40 \times 40/2 \times 40/2$ points and six levels with non-moving boxes of $80 \times 80/2 \times 80/2$ points (the divisions by 2 are due to using quadrant symmetry). The resolution at the finest level ($l = 10$ in this case) is $h_{10} = M/56.9$ and the outer boundary is placed at $\sim 729M$ from the origin.

Finally, we note that BAM is MPI parallelized. When N processors are used, each box on each refinement level is divided into N equally sized sub-boxes with added ghostzones. Each of these sub-boxes is then owned and evolved by one processor. The ghostzones are

Table 2. Grid structure of the χ (C-) and ϕ (P-) runs. The χ (ϕ) runs used $\eta = 2.0/M$ ($\eta = 1.0/M$).

Run	Grid
$C1$	$\chi_{\eta=2}[5 \times 40 : 6 \times 80]\,[h_{10} = M/56.9 : OB = 729M]$
$C2$	$\chi_{\eta=2}[5 \times 44 : 6 \times 88]\,[h_{10} = M/62.6 : OB = 728M]$
$C3$	$\chi_{\eta=2}[5 \times 48 : 6 \times 96]\,[h_{10} = M/68.3 : OB = 727M]$
$C4$	$\chi_{\eta=2}[5 \times 52 : 6 \times 104]\,[h_{10} = M/73.9 : OB = 727M]$
$C5$	$\chi_{\eta=2}[5 \times 56 : 6 \times 112]\,[h_{10} = M/79.6 : OB = 726M]$
$P1$	$\phi_{\eta=1}[4 \times 32 : 6 \times 64]\,[h_{9} = M/68.3 : OB = 244M]$
$P2$	$\phi_{\eta=1}[4 \times 40 : 6 \times 80]\,[h_{9} = M/85.3 : OB = 243M]$
$P3$	$\phi_{\eta=1}[4 \times 48 : 6 \times 96]\,[h_{9} = M/102.4 : OB = 243M]$
$P4$	$\phi_{\eta=1}[4 \times 56 : 6 \times 112]\,[h_{9} = M/119.5 : OB = 242M]$
$P5$	$\phi_{\eta=1}[4 \times 32 : 8 \times 64]\,[h_{11} = M/68.3 : OB = 975M]$
$P6$	$\phi_{\eta=1}[4 \times 40 : 6 \times 80]\,[h_{9} = M/160.0 : OB = 130M]$

synchronized in the usual way after each evolution step. In this way, each processor owns exactly one sub-box of every mesh refinement box, which optimizes load balancing since then each processor works on the same number of grid points. For additional details about the version of the BAM code used here, see [12].

We tested the BAM code by running simulations of a high-spin black hole binary system with individual spins $S/m^2 = 0.75$ aligned with the orbital angular momentum. We choose x–y as the binary's orbital plane which leaves the z component of the angular momentum as the only nonzero component of J_V. Table 2 shows the characteristics of the simulations performed for this paper. The runs are grouped in those using χ (C-runs) as the dynamical variable and those using ϕ (P-runs). For the former (latter), we chose a value for the shift parameter η of $2.0/M$ ($1.0/M$). In general, the simulations performed here have higher maximum spatial resolutions than those in [12], showing the moving punctures method's stability even when the coordinate separation between the grid points and the punctures is as small as $M/320$ (run $P6$).[3] Another difference is that the grids used for the C-runs are larger than those of [12]. These extensions of the grid size and high resolutions did not excite any undesirable instabilities; in the case of $C2$, the simulation was run for the equivalent of over 20 orbital periods[4].

One of the strongest characteristics of the BAM code is its ability to perform good quality simulations with modest computer resources. Table 3 shows typical running times and memory requirements for the simulations of table 2. Note that BAM performs faster after the merger, when only one set of non-moving boxes remains. All the simulations presented in this paper were run on dual processor workstations, namely an AMD Dual Opteron 2.2 GHz workstation with 8 Gb of memory and an Intel Dual Xeon 2.6 GHz workstation with 16 Gb. The former computer can be purchased at the time of publication for less than $3000 USD. Note that, while none of the runs presented here required significantly more than 8 Gb of memory, the cost of expanding the workstation memory capabilities has dropped considerably in the last year. Currently, a 1 Gb memory module for our AMD machine retails for about $100 USD.

Evolutions of BBH that start at larger separations would in principle require longer running times and more computer memory. Estimates of how much longer it would take to run extra orbits on any of our example runs can be obtained from the information given in the last column of table 3. The memory requirements, on the other hand, will depend on the grid structure to be used and obviously the location of the outer boundaries. The memory

[3] See [7, 23] for details on the spacetime geometry close to the punctures.
[4] Assuming a nominal orbital length of $114M$, obtained from the initial data set angular velocity.

Table 3. Typical performance of the BAM code on an AMD Dual Opteron 2.2 GHz workstation (runs $P4$, $C1$, $C3$ and $C5$) and an Intel Dual Xeon 2.6 GHz workstation (runs $P1$, $P2$, $P3$, $P5$ and $C4$). While these workstations are by themselves not particularly expensive, they were fitted with 8 Gb (opteron) and 16 Gb (xeon) of memory that increased their cost significantly. The last column shows the time (in days) it takes to evolve for one orbit using a nominal orbital length of $114M$, obtained from the initial data set angular velocity. Due to the loss of the files, $P6$ performance could not be estimated. $LC5$ corresponds to a simulation identical to $C5$ but performed using the LEAN code [37]. The last row (FG) corresponds to a simulation using full grid presented in [42].

Run	Mem (Gb)	Pre-merger ($M\,\mathrm{h}^{-1}$)	Post-merger ($M\,\mathrm{h}^{-1}$)	One orbit
$C1$	4.2	10.8	17.8	$0.44d$
$C2$	5.5	7.7	12.9	$0.62d$
$C3$	6.3	5.2	9.4	$0.91d$
$C4$	7.7	3.6	6.6	$1.32d$
$C5$	8.1	3.1	5.8	$1.53d$
$P1$	4.1	7.2	10.1	$0.66d$
$P2$	4.3	6.8	9.8	$0.70d$
$P3$	4.9	6.2	9.1	$0.78d$
$P4$	8.2	1.7	3.1	$2.79d$
$P5$	4.6	6.4	9.0	$0.74d$
$LC5$	6.5	2.3	4.6	$2.07d$
FG	11.7	2.3	4.6	$2.20d$

requirements for runs such as ours would not change as long as the separation distance is not increased to more than $9.5M$, which would yield an initial orbital period of more than $200M$, thus leading to several more orbits before merger. The runs described in table 2 were performed using quadrant symmetry. However, generic BBH with arbitrary masses and spins have to be simulated in full grids which, all things kept equal, would require about four times more memory and execution time. These requirements, however, can be reduced by adopting a different grid geometry. In Tichy and Marronetti [42], generic BBH runs were performed using a grid $\chi_{\eta=2}[5 \times 48 : 5 \times 54]\,[h_9 = M/56.9 : OB = 240M]$. The performance details of one of these runs (completed on the Dual Intel workstation) have been added in the last row of table 3 where we see that, while slower than the previous runs, this simulation only takes a couple of days of execution time per orbit.

Finally, we performed the following comparisons. Firstly, we performed run $C5$ also on a supercomputer (Cray XT3 MPP system at the Pittsburgh Supercomputer Center) using 32 processors. The execution on this machine was about seven times faster ($20\ M\ \mathrm{h}^{-1}$) than on our AMD Dual Opteron workstation. Secondly, we have also evolved model $C5$ of table 2 with the LEAN code [37]. Because quadrant symmetry is not implemented in the current version of the grid driver of the LEAN code, this simulation was performed using equatorial symmetry, but using four processors. The results are listed as $LC5$ in table 2. We emphasize a few caveats in this last comparison. For instance, it was not possible to use identical grid setups due to the different types of symmetries used and the use of cell-centred and vertex-centred grids in BAM and LEAN, respectively. Furthermore, the codes continue to undergo further development with likely improvements, in particular in the case of memory usage in BAM. Finally, the results are likely to be affected by the inclusion of further diagnostic tools, such as horizon finding. However, BAM and LEAN's performance are similar, both in terms of memory usage and speed, indicating that the critical aspect of these codes efficiency is the particular grid structure, more than in intrinsic coding details of the evolution equations.

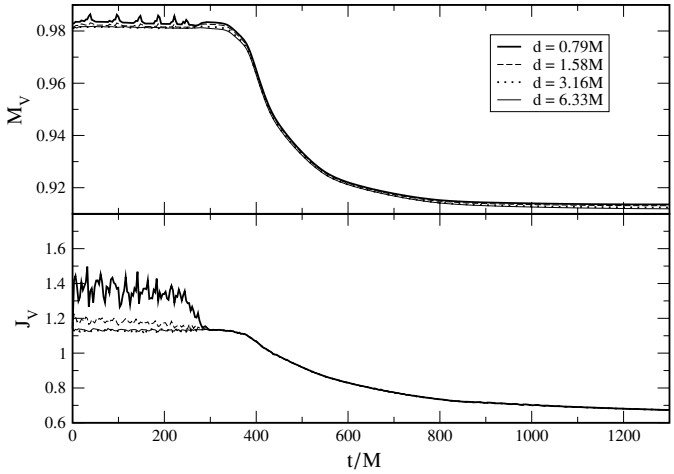

Figure 2. Comparison of M_V and J_V for different inner surfaces. The curves correspond to run $C5$. The side of the inner surface cube is denoted by d.

Table 4. Values of the mass M_V and angular momentum J_V at the time the simulations from table 2 were stopped (t_F). The merger time (t_M) is estimated from the time when the minimum value of the lapse drops below 0.3. The error bars are estimated from the variation in the last $100M$. Due to the loss of the files, $P6$ merger time could not be estimated.

Run	M_V/M	J_V/M^2	$J_V/{M_V}^2$	t_F/M	t_M/M
$C1$	0.914 ± 0.002	0.575 ± 0.005	0.688	1582	262
$C2$	0.914 ± 0.001	0.567 ± 0.003	0.679	2371	262
$C3$	0.913 ± 0.001	0.623 ± 0.007	0.749	1511	262
$C4$	0.912 ± 0.001	0.640 ± 0.007	0.784	1518	263
$C5$	0.912 ± 0.001	0.653 ± 0.007	0.787	1594	263
$P1$	0.914 ± 0.001	0.625 ± 0.002	0.748	1368	297
$P2$	0.915 ± 0.001	0.636 ± 0.001	0.760	1911	291
$P3$	0.913 ± 0.001	0.671 ± 0.003	0.805	869	279
$P4$	0.911 ± 0.001	0.682 ± 0.005	0.822	862	276
$P5$	0.917 ± 0.001	0.627 ± 0.004	0.746	1187	292
$P6$	0.915 ± 0.001	0.631 ± 0.006	0.754	928	–

4. Code tests

4.1. Convergence tests

Table 4 indicates the values obtained for the mass and angular momentum at the time the simulations were stopped (t_F). We also present the time of merger, estimated as the moment when the lapse function drops below a threshold value of 0.3. The error bars simply present the change of each quantity in the last 100 M of the simulation (or a nominal value of 0.001, if the change is smaller than this threshold). The C-runs show larger changes in J_V than the P-runs due to the larger grid size used in the former simulations which requires longer evolution times for the volume integrals to settle.

Figure 2 shows a comparison of M_V and J_V for different positions of the inner surface for run $C5$. The length of the inner cube side (d) is varied in multiples of $d = 0.79M$. Note for reference that the coordinate radius of the final black hole is $\sim 0.73M$. The curves obtained for the smallest cube sizes show noise during the pre-merger stages which disappears when

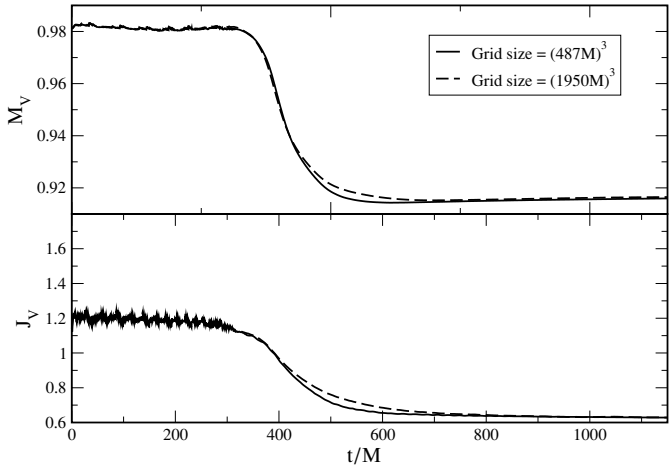

Figure 3. Comparison of M_V and J_V for two runs with different grid sizes. The curves correspond to runs $P1$ (solid) and $P5$ (dashed). $P5$ is identical to $P1$, except for the presence of two additional low resolution outer levels which extend the outer boundaries by a factor of 4.

increasing the cube side. The spikes present at this stage are a numerical artefact caused by the crossing of the moving boxes of the x–z symmetry plane. After the merger, the curves settle to values that agree within a relative error of less than 0.2% for M_V and 0.04% for J_V. This seems to indicate that, when measuring the characteristics of the final black hole, the position of the inner cube does not greatly affect the results.

Figure 3 compares the same quantities for two runs ($P1$ and $P5$) that only differ in the size of the numerical grid. By adding two extra refinement levels to the outside of the grid used for $P1$, we moved the outer boundaries out by a factor of 4. The main difference between these P-runs is the way the curves relax to their final values which agree to within a relative error of 0.01% (0.1%) for M_V (J_V). Again, this seems to show that the size of the grid does not affect significantly the final values of the global quantities.

Figure 4 shows a comparison of runs where the maximum grid resolution has been varied, leaving the rest of the grid characteristics identical. Note that the J_V curves present a downward trend that persists well after the merger. This trend gets less pronounced for higher resolution and might be related to a similar coordinate drift observed in [12]. Figure 5 presents convergence plots for the runs $C2$–$C5$. The runs are grouped in two sets $C2$, $C4$ and $C5$ (thick upper curves) and $C3$, $C4$ and $C5$ (thin lower curves) and their differences are compared and scaled according to a putative fourth-order convergence. The expected fourth-order convergence is approached better by the set with higher resolution.

We also compare two runs with different characteristics but identical maximum grid resolution. The curves from figure 6 correspond to runs $P1$ (solid) and $C3$ (dashed). $P1$ was performed using ϕ as the dynamical variable, equation (1) with $\eta = 1.0/M$ in the recipe for the shift and it had outer boundaries placed at $244M$. $C3$ used χ as the dynamical variable, equation (2) with $\eta = 2.0/M$ and outer boundaries at $727M$. The values of M_V and J_V used for these plots correspond to inner surface cubes of size $6.33M$. As in figure 3, the difference in relaxation is mostly due to the difference in grid sizes. The relative difference between the global quantities at the end of these runs is 0.1% for M_V and 1% for J_V.

Finally, in order to determine the values of the mass and angular momentum for the C-runs of table 2, we used Richardson extrapolation with a polynomial of the type

$$P(h_0) = A_0 + A_1 * h_0^4 + A_2 * h_0^5. \tag{12}$$

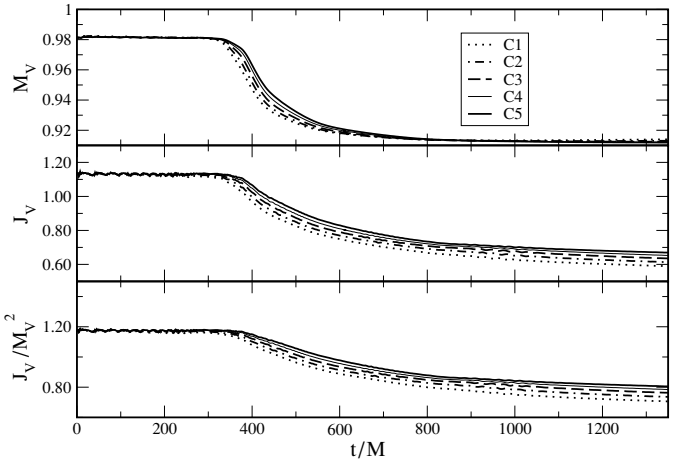

Figure 4. Comparison of M_V and J_V for runs with different grid resolutions. The curves correspond to runs $C1$–$C5$. The values of M_V and J_V used for this test correspond to inner surface cubes of size $6.33M$.

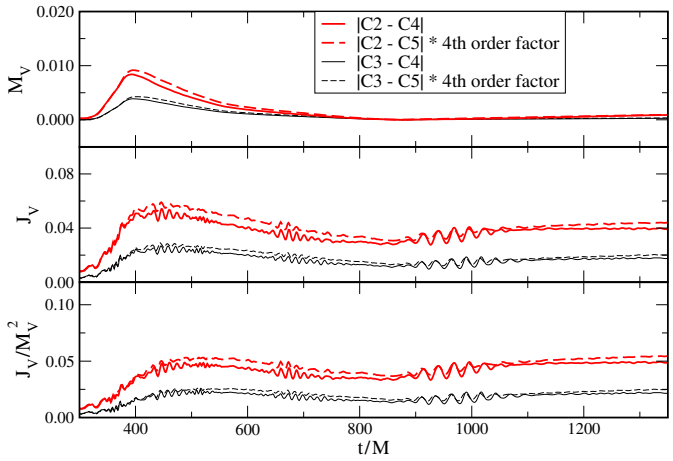

Figure 5. Convergence of M_V and J_V with grid resolution. The curves correspond to runs $C2$–$C5$. The values of M_V and J_V used for these plots correspond to inner surface cubes of size $6.33M$.

Note that this formula assumes fourth-order convergence which, according to figure 5, is only approximate for the runs of this paper. The extrapolation is performed at $t = 1500M$ from runs $C3$, $C4$ and $C5$, giving $M_V = 0.909$ and $J_V = 0.753$. These values agree to within 3% of those reported in [15].

4.2. Comparison of M_V and J_V with alternative estimates of the mass and angular momentum of the final black hole

Alternative estimations of the mass and angular momentum of the final black hole can be derived from evaluating the surface integrals (3), (6) at finite radii. Figure 7 compares the values of M_V and J_V with integrations performed on spherical surfaces at coordinate radii $30M$, $50M$ and $100M$. The mass curves corresponding to the spherical surface integrations

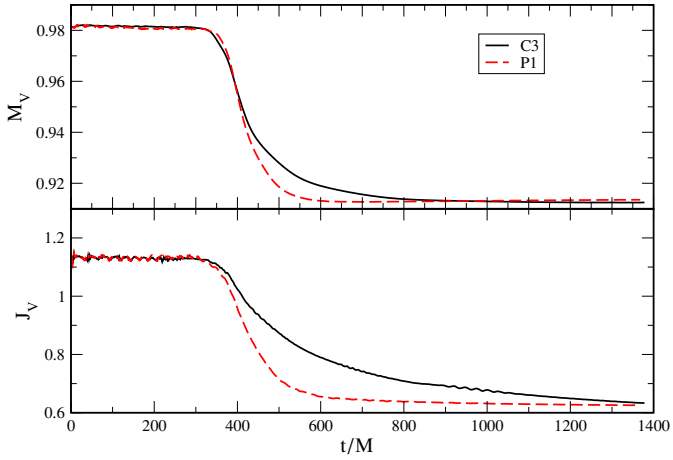

Figure 6. Comparison of M_V and J_V from two runs using the dynamical variables ϕ $(P1)$ and χ $(C3)$.

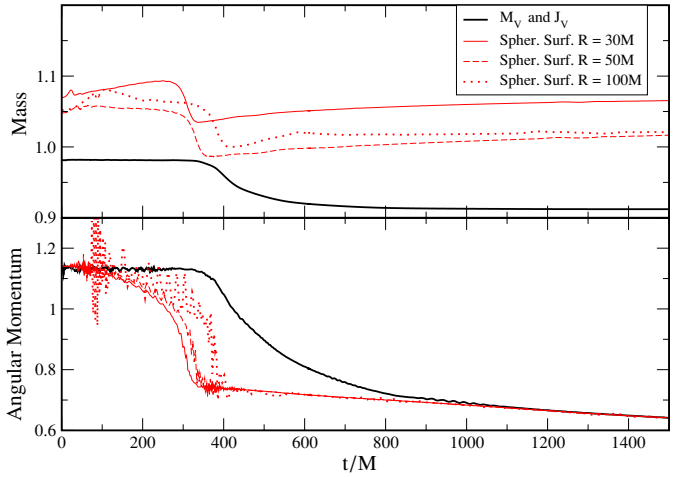

Figure 7. Comparison of M_V and J_V (solid) and spherical surface integrations at radii $30M$ (dotted), $50M$ (dashed) and $100M$ (dashed-dotted). The curves correspond to run $C4$.

have very large errors that behave in a non-systematic way when the extraction radius is increased. At the same time, the calculations of the angular momentum using spherical surface integrals, while noisy before the merger, agree with J_V to within a 0.001% relative error at the end of the simulation.

Figure 8 shows the radiated energy calculated from the flux through spherical surfaces using the Newman–Penrose scalar Ψ_4 (see equation (52) in [12]) at radii $15M$, $30M$, $60M$, $80M$ for run $C4$. From the radiated energy, we generated an estimate for the time evolution of the mass by subtracting those curves from the initial M^{ADM} as reported in table 1 (dashed curves). These curves show a downward drift that is more pronounced with the proximity of the spherical surface to the centre of the grid. The result obtained for radius $80M$ is the one that appears to be the least affected by this effect and it agrees with M_V within a relative error of about 1%.

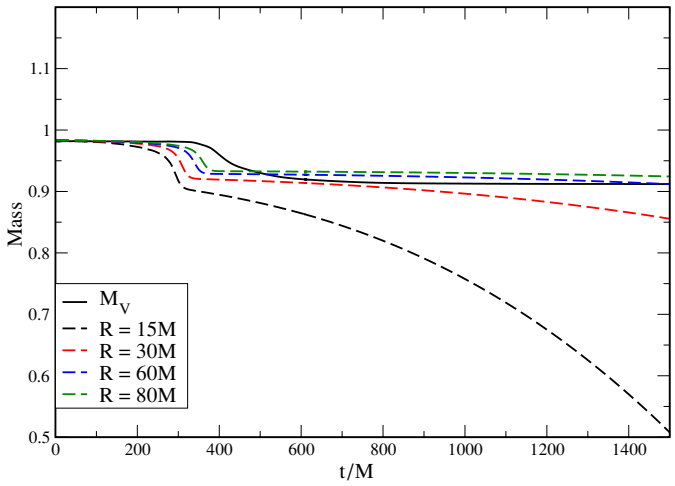

Figure 8. Comparison of M_V (black solid) and mass estimates from the energy radiated through spherical surfaces at different radii (colour dashed). The latter curves were generated by subtracting the radiated energy from the initial M^{ADM}. The curves correspond to run $C4$ and inner surface cube size $6.33M$.

The Christodoulou formula, valid for stationary axisymmetric spacetimes like the Kerr geometry of the final black hole, gives the following relation between the angular momentum J, mass M and irreducible mass of a black hole M_{irr}:

$$J = 2M_{\mathrm{irr}}\sqrt{M^2 - M_{\mathrm{irr}}^2}. \tag{13}$$

Here

$$M_{\mathrm{irr}} = \sqrt{\frac{A_H}{16\pi}}$$

is determined from the proper area A_H of the apparent horizon (for the run $C4 M_{\mathrm{irr}} \approx 0.825M$). We verified relation (13) for several of the runs of table 2 and found it to be satisfied to a relative error of less than 0.2%.

5. Results and conclusions

The main goal of this paper is to show the ability of the BAM code to perform certain simulations of binary black holes with relatively modest computer resources. The simulations presented here were performed on dual processor workstations that have been outfitted with at least 8 Gb of memory. Machines like these retail at the moment of publication for less than $3000 USD, making them easily accessible to any research group.

Our runs were based on the same initial state: one corresponding to two identical black holes with intrinsic spin parameters $S/m^2 = 0.75$ and spins parallel to the orbital angular momentum and which started out at a coordinate separation of $6M$. This data set is similar to the one used by Campanelli *et al* [15]. Our results for the mass and angular momentum of the final black hole agree to within 3% of those of [15]. Better accuracy could be achieved with higher resolution runs, however they would also demand larger computer resources. We are currently testing different grid structures (i.e., varying moving boxes sizes, number, etc) that improve these runs accuracy without increasing the computational burden (see, for instance, [42]). We performed high spatial resolution simulations (of up to $M/160$) and large grid

size (up to outer boundaries at $975M$) to test the moving punctures method's stability and robustness. None of the runs showed any signs of exponentially growing instabilities; they were stopped due to the long real-time duration of the simulations. In one of our test cases, the simulation was run for the equivalent of more than 20 orbital periods.

The simulations discussed in this paper were performed using quadrant symmetry, which require about four times less memory and computer time than non-symmetric scenarios. An improved choice of grid structure can (to some extent) minimize these requirements (see [42], for non-symmetric simulations using workstations). BAM capabilities for efficient use of computer resources permit the exploration of BBH parameter space by enabling low resolution simulations that only require workstations or one or two nodes per run in local Beowulf clusters, where many of such runs can be done simultaneously. Ongoing code optimization is currently enhancing the code performance with regard to memory and CPU usage. Nevertheless, it is clear that today's most demanding binary simulations still require supercomputer resources. However, given the rapid growth of computer power and high efficiency codes such as BAM, even these simulations might be within the reach of workstation resources in the next couple of years.

Acknowledgments

Special thanks to B Israel for help with running the BAM code. This work was partially supported by NSF grant PHY0555644, National Computational Science Alliance under grants PHY020007N, PHY050010T, PHY050015N and PHY060021P and by DFG grant SFB/Transregio 7 'Gravitational Wave Astronomy'. We thank the DEISA Consortium (co-funded by the EU, FP6 project 508830), for support within the DEISA Extreme Computing Initiative (www.deisa.org); code development was also performed at LRZ Munich and HLRS, Stuttgart. JG and US acknowledge support from the ILIAS Sixth Framework Programme.

References

[1] Alcubierre M, Brügmann B, Diener P, Koppitz M, Pollney D, Seidel E and Takahashi R 2003 Gauge conditions for long-term numerical black hole evolutions without excision *Phys. Rev.* D **67** 084023

[2] Ansorg M, Brügmann B and Tichy W 2004 A single-domain spectral method for black hole puncture data *Phys. Rev.* D **70** 064011

[3] Baker J G, Centrella J, Choi D, Koppitz M and van Meter J 2006 Gravitational wave extraction from an inspiraling configuration of merging black holes *Phys. Rev. Lett.* **96** 111102

[4] Baker J G, Centrella J, Choi D, Koppitz M and van Meter J 2006 Binary black hole merger dynamics and waveforms *Phys. Rev.* D **73** 104002

[5] Baker J G, Centrella J, Choi D I, Koppitz M, van Meter J R and Miller M C 2006 Getting a kick out of numerical relativity *Astrophys. J.* **653** L93 (*Preprint* astro-ph/0603204)

[6] Baumgarte T W and Shapiro S L 1999 Numerical integration of Einstein's field equations *Phys. Rev.* D **59** 024007

[7] Baumgarte T W and Naculich S G 2007 Analytical representation of a black hole puncture solution *Phys. Rev.* D **75** 067502 (*Preprint* gr-qc/0701037)

[8] Berger M J and Oliger J 1984 Adaptive mesh refinement for hyperbolic partial differential equations *J. Comput. Phys.* **53** 484–512

[9] Bowen J M and York J W Jr 1980 Time-symmetric initial data for black holes and black hole collisions *Phys. Rev.* D **21** 2047

[10] Brandt S and Brügmann B 1997 A simple construction of initial data for multiple black holes *Phys. Rev. Lett* **78** 3606

[11] Brügmann B, Tichy W and Jansen N 2004 Numerical simulation of orbiting black holes *Phys. Rev. Lett.* **92** 211101

[12] Brügmann B, Gonzalez J, Hannam M, Husa S, Sperhake U and Tichy W 2006 Calibration of moving puncture simulations *Preprint* gr-qc/0610128

[13] Campanelli M, Lousto C O, Marronetti P and Zlochower Y 2006 Accurate evolutions of orbiting black-hole binaries without excision *Phys. Rev. Lett.* **96** 111101
[14] Campanelli M, Lousto C O and Zlochower Y 2006 The last orbit of binary black holes *Phys. Rev.* D **73** 061501
[15] Campanelli M, Lousto C O and Zlochower Y 2006 Gravitational radiation from spinning-black-hole binaries: the orbital hang up *Phys. Rev.* D **74** 041501
[16] Campanelli M, Lousto C O and Zlochower Y 2006 Spin-orbit interactions in black-hole binaries *Phys. Rev.* D **74** 084023
[17] Campanelli M, Lousto C O, Zlochower Y, Krishnan B and Merritt D 2007 Spin flips and precession in black-hole-binary mergers *Phys. Rev.* D **75** 064030 (*Preprint* gr-qc/0612076)
[18] Duez M D, Marronetti P, Shapiro S L and Baumgarte T W 2003 Hydrodynamic simulations in 3+1 general relativity *Phys. Rev.* D **67** 024004
[19] Duez M D 2001 Private communications
[20] Font J A and Ibanez J M 1998 Non-axisymmetric relativistic Bondi–Hoyle accretion onto a Schwarzschild black hole *Mon. Not. R. Astron. Soc.* **298** 835
[21] Font J A, Ibanez J M and Papadopoulos P 1998 A 'horizon adapted' approach to the study of relativistic accretion flows onto rotating black holes *Astrophys. J.* **507** L67
[22] Gonzalez J A, Sperhake U, Brügmann B, Hannam M and Husa S 2007 Total recoil: the maximum kick from nonspinning black-hole binary inspiral *Phys. Rev. Lett.* **98** 091101 (*Preprint* gr-qc/0610154)
[23] Hannam M, Husa S, Pollney D, Brügmann B and O'Murchadha N 2006 Geometry and regularity of moving punctures *Preprint* gr-qc/0606099
[24] Herrmann F, Hinder I, Shoemaker D and Laguna P 2007 *Class. Quantum Grav.* **24** S33 (*Preprint* gr-qc/0601026)
[25] Jansen N, Brügmann B and Tichy W 2006 Numerical stability of the AA evolution system compared to the ADM and BSSN systems *Phys. Rev.* D **74** 084022
[26] Kidder L E 1995 Coalescing binary systems of compact objects to postNewtonian 5/2 order: V. Spin effects *Phys. Rev.* D **52** 821
[27] Marronetti P, Duez M D, Shapiro S L and Baumgarte T W 2004 Dynamical determination of the innermost stable circular orbit of binary neutron stars *Phys. Rev. Lett.* **92** 141101
[28] Marronetti P 2005 Hamiltonian relaxation *Class. Quantum Grav.* **22** 2433
[29] Marronetti P 2006 Momentum constraint relaxation *Class. Quantum Grav.* **23** 2681
[30] O'Murchadha N and York J W Jr 1974 *Phys. Rev.* D **10** 2345
[31] Press W H, Teukolsky S A, Vetterling W T and Flannery B P 1992 *Numerical Recipes in Fortran* (Cambridge: Cambridge University Press) p 127
[32] Pretorius F 2005 Evolution of binary black hole spacetimes *Phys. Rev. Lett.* **95** 121101
[33] Pretorius F 2006 Simulation of binary black hole spacetimes with a harmonic evolution scheme *Class. Quantum Grav.* **23** S529
[34] Schnetter E, Krishnan B and Beyer F 2006 Introduction to dynamical horizons in numerical relativity *Phys. Rev.* D **74** 024028
[35] Shibata M and Nakamura T 1995 Evolution of three-dimensional gravitational waves: harmonic slicing case *Phys. Rev.* D **52** 5428
[36] Shibata M 1999 Fully general relativistic simulation of coalescing binary neutron stars: preparatory tests *Phys. Rev.* D **60** 104052
[37] Sperhake U 2006 Binary black-hole evolutions of excision and puncture data *Preprint* gr-qc/0606079
[38] Tichy W, Brügmann B, Campanelli M and Diener P 2003 Binary black hole initial data for numerical general relativity based on post-Newtonian data *Phys. Rev.* D **67** 064008
[39] Tichy W, Brügmann B and Laguna P 2003 Gauge conditions for binary black hole puncture data based on an approximate helical Killing vector *Phys. Rev.* D **68** 064008
[40] Tichy W and Brügmann B 2004 Quasi-equilibrium binary black hole sequences for puncture data derived from helical Killing vector conditions *Phys. Rev.* D **69** 024006
[41] Tichy W 2006 Black hole evolution with the BSSN system by pseudo-spectral methods *Phys. Rev.* D **74** 084005
[42] Tichy W and Marronetti P 2007 Binary black hole mergers: large kicks for generic spin orientations *Preprint* gr-qc/0703075
[43] Yo H J, Baumgarte T W and Shapiro S L 2002 Improved numerical stability of stationary black hole evolution calculations *Phys. Rev.* D **66** 084026
[44] Yunes N and Tichy W 2006 Improved initial data for black hole binaries by asymptotic matching of post-Newtonian and perturbed black hole solutions *Phys. Rev.* D **74** 064013
[45] Yunes N, Tichy W, Owen B J and Brügmann B 2006 Binary black hole initial data from matched asymptotic expansions *Phys. Rev.* D **74** 104011